

Confining iron oxide nanocubes inside submicrometric cavities as a key strategy to preserve magnetic heat losses in an intracellular environment

Mikhail V. Zyuzin^{1,2}, Marco Cassani^{1,3}, Markus J. Barthel¹, Helena Gavilan¹, Niccolò Silvestri^{1,3}, Alberto Escudero⁴, Alice Scarpellini¹, Federica Lucchesi^{1,5}, Francisco J. Teran^{6,7}, Wolfgang J. Parak^{8*}, Teresa Pellegrino^{1*}.

1. Istituto Italiano di Tecnologia, Via Morego 30, 16163 Genova, Italy.
2. Faculty of Physics and Engineering, ITMO University, Lomonosova 9 St. Petersburg, Russia
3. Dipartimento di Chimica, Università di Genova, Via Dodecaneso 33, 16146 Genova, Italy
4. Leibniz Institute for New Materials. Campus D2 2. D-66123 Saarbrücken, Germany
5. Dipartimento di Informatica, Bioingegneria, Robotica e Ingegneria dei Sistemi (DIBRIS), Via all'Opera Pia, 13, 16145, Genova
6. iMdea Nanociencia, Campus Universitario de Cantoblanco, 28049 Madrid, Spain
7. Nanobiotecnología (iMdea-Nanociencia), Unidad Asociada al Centro Nacional de Biotecnología (CSIC), 28049 Madrid, Spain
8. Faculty of Physics and Chemistry and CHyN, Universität Hamburg, Hamburg, Germany

* corresponding authors: wolfgang.parak@uni-hamburg.de and teresa.pellegrino@iit

Abstract

The design of magnetic nanostructures whose magnetic heating efficiency remains unaffected at the tumor site is a fundamental requirement to further advance magnetic hyperthermia in clinic. This work demonstrates that the confinement of magnetic nanoparticles (NPs) into a submicrometric cavity is a key strategy to enable a certain degree of nanoparticle motion and minimize aggregation effects, consequently preserving the magnetic heat loss of iron oxide nanocubes (IONCs) under different conditions, including intracellular environments. We fabricated magnetic Layer-by-Layer (LbL) self-assembled polyelectrolyte submicrometric capsules using three different approaches, and we studied their heating efficiency as obtained in aqueous dispersions and once internalized by tumor cells. First, IONCs were added to the hollow cavities of LbL submicrocapsules, allowing the IONCs to move to a certain extent in the capsule cavities. Second, IONCs were co-encapsulated into solid calcium carbonate cores coated with LbL polymer shells. Third, IONCs were incorporated within the polymer layers of the LbL capsule walls. In aqueous solution, the higher specific absorption rate (SAR) values were related to the ones of free IONCs, while lower SAR values were recorded for capsule/core assemblies. However, after uptake by cancer cell lines (SKOV-3 cells), the SAR values of the free IONCs were significantly lower than those observed for capsule/core assemblies, especially after prolonged incubation periods (24 and 48 hours). These results show that IONCs packed into submicrocavities preserve the magnetic losses, as SAR values remained almost invariable. Conversely, free IONCs without the protective capsule shell agglomerated and their magnetic losses are strongly reduced. Indeed, IONC loaded capsules and free IONCs reside inside endosomal and lysosomal compartments after cellular uptake, show magnetic losses strongly reduced due to the immobilization and aggregation in centrosymmetrical structures in the intracellular vesicles. The confinement of IONCs into submicrometric cavities is a key strategy to provide a sustained and predictable heating dose inside biological matrices.

Introduction

The therapeutic benefits of heat have been well known for centuries. In oncothermia, it has been shown that raising the temperature (*i.e.* inducing hyperthermia) can be a successful adjuvant therapeutic approach for treating solid tumors in combination with radio- or chemotherapy.^{1,2} Today, nanotechnology provides novel and minimally invasive ways to locally release heat inside a body by means of distinct remote activation modalities.³⁻⁵ Recent studies underline the large benefits and efficiency of spatially controlled heat deposition by magnetic nanoparticles to remove localized tumors.⁵⁻⁸ Among the suitable nanomaterials used in hyperthermia studies, iron oxide nanoparticles (IONPs) are widely employed since their magnetic properties can be precisely controlled.⁹⁻¹¹ They benefit to have negligible toxicity drawbacks, and high biodegradation and clearance capabilities after treatment.^{12,13} The exposure of iron oxide nanoparticles to

alternating magnetic fields and/or infrared radiation leads to heat generation, which has been successfully employed to remove cancer cells.¹⁴ For this reason, enormous efforts have been devoted to the development of nanostructures based on iron oxide nanoparticles with outstanding magnetic losses.^{15,16} Alongside, the emerging technique of magnetic particle imaging (MPI)^{17,18} benefits from iron oxide nanoparticle tracers whose magnetic characteristics are similar to the ones valid for magnetic hyperthermia.¹⁹

Subsequent to the first evidence of hyperthermia that was mediated by microparticles in the fifties,²⁰ many preclinical studies^{6,21–24} and clinical trials^{20,25} over the last 15 years have shown promising results with regard to hyperthermia that is mediated by iron oxide nanoparticles for cancer treatment. Reports on the first clinical trials using iron oxide nanoparticles for treating recurrent glioblastoma multiforme (DRKS00005476 clinical trial) and prostate carcinoma (clinical trial NCT02033447) in magnetic hyperthermia have provided the first proof of concept on a human scale, rendering the introduction of magnetic hyperthermia to clinics as the main research task today.²⁵ For this purpose, it is necessary to control the heat dose inside tumors, a highly relevant clinical requirement. Some efforts have been spent to produce magnetic nanoparticles that possess outstanding heat efficiency in highly viscous environment.^{26,27} Despite this, recent studies have evidenced that the magnetic properties of nanoparticles are dramatically altered in different biological environments.^{9,18,28,29} In particular, the magnetic heat losses from iron oxide nanoparticles in cellular environments suffer significant reductions ranging from 70% to 90% depending on nanoparticle size, chemical composition, and/or aggregation degree.⁹ Recent results show that the enhancement of nanoparticle immobilization in an intracellular environment and, in particular, the nanoparticle clustering during the intracellular transit alter the magnetic behavior under alternating magnetic fields immediately after cell uptake.³⁰ These results demonstrate that hyperthermia mediated by IONPs behaves differently under *in vitro* and *in vivo* conditions than in colloidal dispersion. For this reason, not only the synthesis protocols of iron oxide nanoparticles need to be improved, but new approaches to preserve the magnetic losses and/or MPI performance of magnetic nanostructures into biological environments (i.e. cells and tissues) are also required.³¹ Recent works have shown that the random confinement of IONP into capsules at fixed inter-particle distances freezes the magnetic dipolar interactions in such a way that the agglomeration effects have no effect on the magnetic losses.^{32,33} Multilayer polyelectrolyte (PE) encapsulation is a cheap and robust Layer-by-Layer (LbL) based approach which consists of the subsequent assembly of oppositely charged polymers that form the capsule's wall when they are deposited onto a sacrificial template.^{34–37} The size of the capsules can be precisely tuned from tens of nanometers to several microns according to the core template and, after the LbL procedure, the sacrificial template can be dissolved so that hollow polyelectrolyte capsules can be obtained.³⁴ The capsules can be loaded with different compounds, like proteins, mRNA, biomolecules, or nanoparticles whose distribution can be located at different places on the capsules (cavity or shells), thus enabling them to protect the cargo from enzymatic degradation.^{38,39}

Here, we report on how the magnetic heat losses of highly performing iron oxide nanocubes (IONCs) with different edge lengths (8, 14, 16, 18 and 21 nm) vary when they are distinctly embedded into the capsules. The magnetic capsules developed here encapsulated IONCs in three different spatial arrangements: i) in the hollow cavity; ii) in a solid CaCO₃ core; iii) in-between the polymer layers of the capsule walls. The magnetic heat losses observed for the different IONCs/capsule arrangements were compared to those of free IONCs under different conditions: in water, in viscous media (water or glycerol dispersions), or upon cellular internalization after different incubation times. Overall, our data suggest that, among the different configurations studied, the spatial confinement of IONCs in the hollow submicrometric cavity is optimal to preserve the magnetic heat losses of IONCs inside cells. Thus, the hollow capsules have sustained and predictable heating efficiency for hyperthermia performances into biological environments.

Experimental section

Materials

Dopamine hydrochloride, sodium nitrite, sulphuric acid, α - ω -hydroxypoly(ethylene glycol) (PEG, M_w = 1400 g/mol), anhydrous dichloromethane (CH₂Cl₂), trimethylamine (TEA), 4-dimethylaminopyridine (DMAP), succinic anhydride, *N*-hydroxysuccinimide (NHS), *N,N'*-dicyclohexylcarbodiimide (DCC), dimethylformamide (DMF), toluene sodium carbonate (Na₂CO₃), calcium chloride dihydrate (CaCl₂ x 2H₂O), ethylene glycol (EG), poly(sodium 4-styrenesulfonate) (PSS, M_w = 70000 g/mol), poly(allylaminehydrochloride) (PAH, M_w = 15000 g/mol), sodium chloride (NaCl), ethylenediaminetetraacetic acid (EDTA), glycerol, and McCoy's 5A medium were purchased from Aldrich and used as received. Ultrapure water or Milli-Q water with a resistance greater than 18.2 M Ω cm⁻¹ was used for all experiments. Dulbecco phosphate buffered saline (DPBS), phosphate buffered saline (PBS), fetal bovine serum (FBS), trypsin-EDTA 1x in PBS, penicillin and streptomycin (P/S), glutaraldehyde buffer, cacodylate buffer, osmium tetroxide, uranyl acetate, ethanol, and epoxy Epon™ (TAAB) resin were purchased from Euro Clone and used as received.

Synthesis of Iron Oxide Nanocubes

IONCs with a cubic shape and different edge length sizes (8, 14, 16, 18, 21 nm) were synthesized according to an already published protocol.⁴⁰ Briefly, iron (III) acetylacetonate (1 mmol) was mixed in a three-neck flask with decanoic acid (the added amount in mmol depends on the expected size) in a solution of dibenzyl ether and squalane. The solution was then degassed at 65 °C for 2 hours and was later heated up to 200 °C under nitrogen flow. After 2 hours at 200°C, the solution was heated up by refluxing until it reached a temperature of 305 °C. It was kept at this temperature for 1 hour. The resulting dispersions containing the formed IONCs were cooled down to room temperature (RT), centrifuged so as to remove the supernatants (8500 rpm for

10 min) and washed twice with acetone (*i.e.* acetone was added, and the supernatants were removed after centrifugation). The IONCs were finally dispersed in chloroform (Figure S1).

Synthesis of α -nitrodopamine- ω -carboxypoly(ethylene glycol) (ND-PEG-COOH) as a water transfer ligand

α -nitrodopamine- ω -carboxy-poly(ethylene glycol) (ND-PEG-COOH) was chosen as a water transfer ligand for the nanocubes. We adapted already existing procedures for the synthesis of the nitrodopamine modified carboxyl terminated poly(ethylene glycol) (Figure 1 and Figures S2-S5 and Scheme S1 of the electronic supporting information, ESI).^{40,41} The synthesis was carried out in four steps. First, nitrodopamine was obtained by nitrating the aromatic ring of the dopamine molecule, as described in literature but with minor modifications.⁴⁰ In parallel, a α - ω -hydroxy-poly(ethylene glycol) was reacted with succinic anhydride (1:2 ratio) in order to transform the hydroxyl into carboxy functions. Subsequently, one terminal carboxy group of the PEG was activated using DCC/NHS chemistry, then nitrodopamine was coupled to the polymer following a reported protocol.⁴¹ A detailed synthesis of the polymeric ligand and the characterization is shown in the ESI.

Ligand exchange and water transfer of cubic iron oxide nanoparticles (IONCs)

A well-established protocol for the water transfer of IONCs was used with minor modifications. The procedure is described for 18 nm edge size IONCs and is representative for all other samples in terms of the stoichiometry.^{41,42} In detail, 1.88 mL of chloroform was added to 2.12 mL of the IONC dispersion in chloroform, which contained 4 mg of Fe, yielding a final concentration of 1 g/L Fe. ND-PEG-COOH was used as a hydrophilic ligand for the water transfer. For this, a ratio of 150 ligands/nm² per IONC's surface was applied. 121 mg of the polymeric ligand (0.086 mmol) were dissolved in 1.61 mL of chloroform, yielding in a polymer solution with a final concentration of 0.05 M. Both mixtures (the polymeric ligand and the suspension containing the IONCs) were mixed in a glass vial, and 0.79 mL of TEA (70 eq. with regard to mmol of ligands) was added. The mixture was vigorously shaken overnight at room temperature (RT) to allow the initial hydrophobic ligands to be replaced with the hydrophilic ND-PEG-COOH, causing the nitrodopamine to act as an anchor. Subsequently, 40 mL of toluene was added and the mixture was transferred into a separatory funnel. 100 mL of MilliQ water was added, and the mixture was shaken to form an emulsion and to induce the water transfer of the nanoparticles. The aqueous phase containing the first fraction of nanoparticles was collected, 50 mL of water was added to the organic phase, and the procedure was repeated so as to extract the remaining nanoparticles. Afterwards, both aqueous phases were combined, and possible traces of remaining toluene were removed using a nitrogen flow. The sample was concentrated to a final volume of approximately 10 mL by centrifugation using an amicon centrifuge filter (50000 g/mol cut-off, 1500 rpm). This dispersion was sonicated for 30 min at 65 °C with the purpose of redispersing the cubic IONCs. The sample was transferred into a spectrum labs dialysis membrane bag (cut-off 100000 g/mol, 1700 rpm), and

the mixture was dialyzed against water for 2 days for purification. The purified sample was concentrated two times using an amicon centrifuge filter until a final volume of approximately 2 mL was obtained. The sample was then sonicated again for 30 min at 65 °C. The final product was analyzed by dynamic light scattering (DLS) measurements (Figures S6-S9, Table S1).

Nanoparticle characterization

The colloidal stability of PEG-coated IONCs was studied by monitoring the hydrodynamic diameter in different media with DLS. The nanoparticles were dispersed in MilliQ water, a 0.33 M calcium chloride solution, a 0.33 M sodium carbonate solution, a 0.2 M ethylenediaminetetraacetic acid solution, and in full cell growth medium. Both, the hydrodynamic diameter (D_h , which is given as the mean value of the number, intensity and volume distribution) and the zeta potential (ζ) of the IONCs were measured using a Zetasizer Nano ZS90 (Malvern, US) equipped with a 4.0 mW He–Ne laser operating at 633 nm and with an avalanche photodiode detector, in the 173° backscattered mode. Before the measurements, the samples were highly diluted in an aqueous solution. The measurements were performed at 25 °C. Measurements for each sample were repeated three times, and each measurement included 10 runs for 10 s. Significant increase in the hydrodynamic diameter was an indicator of nanoparticle aggregation.⁴³

The effect of the possible aggregation of the nanoparticles on their magnetic properties was studied for both, free and encapsulated IONCs. The different encapsulated IONCs were mixed at a ratio of 1:1 with 5x PBS until a final concentration of 0.75 g(Fe)/L was reached. Magnetization curves were then measured at a frequency (f) of 100 kHz and a magnetic field (H) of 24 kA/m ($B = 30$ mT) in water and 5x PBS, 0.05 M.

Synthesis of magnetic polyelectrolyte capsules

Synthesis of CaCO₃ cores loaded with IONCs of different sizes

Iron oxide nanocubes (IONCs) with cube-edges of different lengths were encapsulated in submicrometric calcium carbonate cores or embedded into the capsule walls using a modified protocol.⁴⁴⁻⁴⁶ Briefly, 0.33 M calcium chloride and sodium carbonate solutions were prepared in an 5:1 in volume of EG:H₂O mixture. 50 μ L of the water suspensions of the 8,14, 16, 18 and 21 nm IONCs ($c = 3$ g(Fe)/L) was added to 2 mL of the 0.33 M CaCl₂ solution under magnetic stirring. Then, 386 μ L of 0.33 M Na₂CO₃ was added and mixed by stirring vigorously at 1100 rpm for 20 min at room temperature. The formed submicrometric calcium carbonate cores with encapsulated IONCs (8,14, 16, 18, 21 nm) were then centrifuged (at 9000 rpm for 3 min), and the supernatants were discarded. The cores were then washed twice with MilliQ water (*i.e.* addition of water, centrifugation at 9000 rpm for 3 min and then removal of the supernatant). The CaCO₃ cores that were loaded with the different IONCs were then coated with non-biodegradable polyelectrolytes, namely poly(styrene sulfonate) (PSS) and poly(allylamine hydrochloride) (PAH). Polyelectrolytes solutions with a concentration of 10 mg/mL were prepared in 0.05 M sodium chloride, adjusting the pH of the solution to 6.5. CaCO₃ cores

were first dispersed in 1 mL of a 10 mg/mL PSS solution, then sonicated for 5 min, and shaken for 10 min. The cores were then washed twice with MilliQ water at 9000 rpm for 3 min to remove any excess polyelectrolytes. Then, 1 mL of a 10 mg/mL polycationic PAH solution was added to the cores. The dispersion was sonicated again for 5 min, and shaken for 10 min. This procedure was repeated 8 times in order to obtain 8 monolayers (4 bilayers) of shell around the CaCO₃ cores. Finally, the cores with immobilized IONCs in the CaCO₃ matrix coated with 4 bilayers of polyelectrolytes (**CORES**) were obtained. The sample was kept at an iron concentration of 2 mg(Fe)/mL.

Synthesis of capsules loaded with different sized IONCs

Empty multilayer polyelectrolyte submicrometric capsules were obtained by treating the previously prepared iron oxide CaCO₃ cores with 1 mL of EDTA (0.2 M, pH 6). For this, as obtained cores were spun down at 9000 rpm for 3 min. Supernatants were then removed and EDTA was added and dispersions were kept overnight in a shaker at room temperature. The polyelectrolyte capsules were then washed two times with MilliQ water at 1500 rpm for 30 min. At the end of the procedure, capsules with IONCs in the cavity (**CAPS**) were obtained.

Synthesis of capsules with IONCs embedded in their walls

In order to obtain polyelectrolyte capsules with IONCs (8,14, 16, 18, 21 nm) embedded in the capsule wall, bare calcium carbonate cores (with no IONCs) were prepared by directly mixing 2 mL of a 0.33 M calcium chloride solution with 386 μ L of a 0.33 M sodium carbonate solution, both of which were prepared in a 5:1 parts invol. EG:H₂O mixture, in a similar way to the aforementioned procedure,^{38,39} but without the IONCs. Two bilayers of polyelectrolytes were deposited onto the cores in the same way described above, and the IONCs were incorporated after the second PAH layer by adding 50 μ L of IONCs (3 g(Fe)/L) to the CaCO₃ assemblies, then sonicating them (for 5 min), shaking them (for 10 min at room temperature) and washing them. Afterwards, three extra monolayers of polyelectrolytes (PAH/PSS/PAH) were deposited by following the same strategy that was mentioned above. After the deposition of the last polyelectrolyte layer (PAH, 1 mL, 10 mg/mL in 0.05 M NaCl) and the dissolution of the CaCO₃ template (EDTA, 1 mL, 0.2 M, pH 6), capsules with IONCs embedded in the walls (**WALL**) were obtained.

Structural characterization

Transmission electron microscopy (TEM) images were collected with a Jeol JEM 1011 (Jeol, Japan) electron microscope (Electron Microscopy Facility – Fondazione Istituto Italiano di Tecnologia) operating at an acceleration voltage of 100 kV, and recorded with a 11 Mp fiber optical charge-coupled device (CCD) camera (GatanOrion SC-1000). For the sample preparation, 3 μ L of the diluted sample was dropped onto a carbon-coated copper grid, and the solvent was removed by evaporation at room temperature.

In order to perform a TEM analysis on SKOV-3 cells with internalized magnetic materials, previously seeded cells in 18 mm diameter cell culture chambers (10^5 per well) were incubated with 14 nm free IONCs, capsules that had IONCs in the cavity (CAPS), or capsules with IONCs embedded in the wall (WALL) for 24 hours. Afterwards, the cells were fixed for 2 hours in a fixative solution (2% Glutaraldehyde in buffer Na-Cacodylate 0.1M) and were further post-fixed (2 h) in a solution of 1% OsO_4 in a 0.1 M Na-cacodylate buffer. Subsequently, samples were stained overnight in a 1% Uranyl acetate aqueous solution at 4 °C to better highlight the polymer and cellular sub-compartments. After several washes in water, the samples were completely dehydrated with Ethanol and then infiltrated with epoxy Epon™ (TAAB) resin. Once the resin was hardened for 48 h in an oven at 65 °C, 70 nm thick sections were cut with a Leica EMU C6 ultra-microtome. High-resolution scanning electron microscopy (SEM) imaging was carried out using a JEOL JSM 7500FA (Jeol, Tokyo, Japan) equipped with a cold Field Emission Gun, operating at an acceleration voltage of 10 kV. When necessary, the samples were carbon coated with a 10 nm thick film using an Emitech K950X high vacuum turbo system (Quorum Technologies Ltd, East Sussex - UK). The samples were observed using both a secondary electron detector, in order to enhance the topography, and a backscattered electron detector (which is sensitive to differences in molecular weight) in order to detect and show the presence of the IONCs within the capsules.

Representative bright field images were taken with a Nikon A1, CFI Plan Apo VC 60x Oil objective confocal microscope.

To estimate the amount of iron and calcium in the synthesized samples, inductively coupled plasma optical emission spectrometry (ICP-OES) measurements were performed using an iCAP 6000 Series spectrometer (Thermo Scientific). Briefly, 10 μL of the stock core/capsule samples with IONCs was dissolved in 1 mL of aqua regia overnight. After adding MilliQ water until a volume of 10 mL was reached, the solution was filtered with a 0.45 μm PTFE filter and the sample was analyzed. In order to estimate the concentration of iron in the cell-associated magnetic materials, 10 μL of the sample was dispersed in 375 μL of a $\text{HNO}_3\text{:H}_2\text{O}_2$ (vol. 2:1) mixture, which was then sonicated at 65 °C for 2 h. Subsequently, 750 μL of HCl was added, and the samples were digested overnight. The next day, after adding MilliQ water until a volume of 10 mL was reached, the solution was filtered with a 0.45 μm PTFE filter and elemental analysis was performed. =

Magnetic characterization

The magnetic characterization of the synthesized magnetic materials was performed under an alternating magnetic field (AMF) in colloidal dispersions (50 μL at a concentration of 1.5 g(Fe)/L) at different frequencies (50, 100, and 200 kHz) and constant magnetic field amplitude (24 kA/m). AC hysteresis loops were traced at room temperature with a home-made inductive magnetometer built by the Advanced Instrumentation Unit (iMdea Nanociencia, Madrid, Spain) based on the one described by Connord et al.⁴⁷. The magnetic field was generated by a Litz wire solenoid, inside which two counterwise-wound coils with the same diameter and

number of turns collected the induction signal of the sample. The AC magnetization signal was calibrated by comparing magnetization values at similar field intensities which were obtained under AC and quasi-static magnetic field conditions. The AC magnetization signal was normalized to the mass of magnetic material employed in each experiment.

SAR measurements in water and in glycerol (36%, 81%)

The specific adsorption rate (SAR) values of free IONCs, CORES, CAPS, and WALL samples were measured in water and in glycerol (36%, 81%) using a commercially available DM 100 Series (nanoscale Biomagnetics Corp.) setup. 100 μ L of each sample ($c \approx 1.5$ g(Fe)/L) was introduced to the instrument holder and exposed to frequencies of 185 or 302 kHz under magnetic field amplitudes of 28, 24, or 40 kA/m (the latter one only for the frequency 185 kHz). A magnetic field was applied for approximately 60 seconds, and all measurements were repeated 3 times. The specific absorption rate of all the samples was calculated according to the equation:

$$SAR \left[\frac{W}{g} \right] = \frac{C \cdot m_d}{m_{mag}} \frac{dT}{dt}$$

in which C is the specific heat capacity of solvent ($C(\text{water})=4,185$ J/(g·K), $C(\text{glycerol } 36\%) = 3,552$ J/(g·K), $C(\text{glycerol } 81\%) = 2,659$ J/(g·K), $C(\text{cells}) = 4,125$ J/(g·K)), m_d is the mass of the colloidal dispersion, and m_{mag} is the mass of the magnetic material (i.e. iron) in g.¹² The experimental values of the slope of the temperature curve (dT/dt) were measured within the first 10 seconds after the magnetic field was applied to the concentrated magnetic material solution to compensate the non-adiabatic conditions of measurements.

The SAR values for each sample are calculated based on the average of three independent measurements. Generally, SAR values are obtained by calorimetric methods allowing the quantification of MNP heat dissipation losses. However, calorimetry measurements are inaccurate and difficult to standardize.^{48,49} At the same time, the calorimetry method requires to quantify physical parameters from the study system, such as specific heat, which are difficult to be precisely determined in biological matrices (i.e. cells, or tissues) without affecting their integrity. In contrast, AC magnetometry affords a direct and accurate method to probe and quantify the heat release associated with magnetic losses by measuring hysteresis loops under H_{AC} conditions and considering that $SAR= A \cdot f$,⁵⁰ where A is the area enclosed by the hysteresis loop and f is the field frequency.

Cell culture

Ovarian carcinoma cells (SKOV-3) were obtained from the American Type Culture Collection (ATCC) and maintained in a McCoy's 5A Medium, supplemented with 10% fetal bovine serum (FBS) and 1% penicillin/streptomycin (P/S) at 37 °C and 5% CO₂.

Hyperthermia measurements with cells in suspension

The heating abilities under magnetic stimulation of free IONCs, CORES, CAPS, and WALL samples (d(IONCs)=14, 18 nm) once internalized by the SKOV-3 cells were measured. Briefly, 20 million SKOV-3 cells grown in a tissue culture T-75 flask were trypsinized, centrifuged (1500 rpm, 5 min) and transferred to a test tube with a final volume of 50 µL. The samples were dispersed in cell culture medium (2 g(Fe)/L), and 50 µL of this solution was added to the dense cell suspension. The SAR values of the magnetic materials were then measured at different time points (0, 15, 45, 90, and 180 min) under hyperthermia conditions at 302 kHz and 24 kA/m. After the hyperthermia measurements, amounts of iron associated with cells were determined for all the samples by performing an ICP analysis.

Hyperthermia measurements with adherent cells

20 million SKOV-3 cells were seeded per culture plate. The next day, 100 µL of free IONCs (d(IONCs)=14, 18 nm), CAPS, or WALL samples were added to the cells and incubated for 24 and 48 h at 37 °C and with 5% CO₂. The iron concentration was 2 g(Fe)/L in all cases. The cells were then washed 2 times with DPBS, and they were detached from the cell culture flask using 6 mL trypsin-EDTA for 2 min. After adding 18 mL of cell culture medium, the cells were centrifuged at 1500 rpm for 5 min. The supernatant was then removed, and the cells were counted using a NucleoCounter® NC-100™ (ChemoMetec). Reagent A100 (which acts as a lysis buffer) and Reagent B (which acts as a stabilizing buffer) were added to the test tube for the total cell count (cells/mL). The cell pellet with internalized magnetic materials was transferred to a test tube, and the final volume was ca. 100 µL. Heating performances of all samples were measured at 302 kHz and 24 kA/m. After hyperthermia measurements, the iron content associated to the cells was determined for all the samples by performing an ICP analysis.

Results and discussion

IONCs of different sizes (8±1, 14±3, 16±2, 18±2 and 21±2nm) were synthesized for the present study (Figure 1 A, I and F, Figure S10-S11). As the pristine IONCs are covered with a hydrophobic surfactant layer, a ligand exchange procedure was first applied in order to transfer the IONCs from chloroform to water (Scheme 1A).¹⁵ α-nitrodopamine-ω-carboxypoly(ethylene glycol) (ND-PEG-COOH, with a molar mass of 1400 g/mol, Figure 1 and Scheme S1), was synthesized using a multistep reaction by slightly modifying an already existing

procedure, and it was used as a carboxyl-PEG terminated ligand exchange molecule.^{40,41} Nuclear magnetic resonance measurements (NMR) confirmed the expected polymer structure and indicated that the obtained materials had a high purity (Figure S2-S5). The obtained mono-carboxyl functionalization degree (f), which was 60%, indicates the presence of a fraction of double functionalized dicarboxylic-PEG chains. The material was used as received, without further purification. This ND-PEG-COOH polymer contains a nitrodopamine moiety that has a high affinity for metal oxide surfaces, while the PEG segment and the terminal carboxylic group ensures water solubility and stability as a result of steric hindrance and charge repulsion respectively. For the water transfer, the IONCs were first mixed with ND-PEG-COOH in chloroform. Subsequently, TEA base was added in order to deprotonate the hydroxyl groups of the nitrodopamine moiety. After shaking overnight, toluene was added to decrease the density of the mixture and the solution was transferred to a separation funnel. Finally, water was added and the IONCs were phase extracted in water. It should be noted that the aqueous samples, once extracted, tended to aggregate during the concentration step. Here, it was crucial to sonicate the mixture at 65 °C before dialysis in the presence of TEA to ensure that the IONCs could be re-dispersed as single NPs. The IONCs that were dispersed in water had a mean hydrodynamic diameter slightly higher than that measured by TEM for all IONCs, and there was no sign of aggregation in water (Table S1, Figures S7-S10, S11, S12-S13 S14). As is to be expected for these water transferred IONCs, ζ -potential measurements revealed a negative surface charge in the range of -21 to -33mV (Figure S14, S15). To embed the IONCs into calcium carbonate cores, we first tested the colloidal stability of the IONCs in a 0.33 M solution of calcium chloride and in a solution of 0.33 M sodium carbonate, both of which are used as precursors for the CaCO₃ core formation. Moreover, the stability of IONCs in a 0.2 M solution of ethylenediaminetetraacetic acid (EDTA), which is used for the dissolution of CaCO₃ cores, was also tested (TableS2). No significant changes in the hydrodynamic diameter were observed when the IONCs were dispersed in the different solutions, except for the Na₂CO₃ solution, in which the nanoparticles had bigger effective hydrodynamic diameters, indicating aggregation. For this reason, to form magnetic CaCO₃ cores, the negatively charged IONCs were dissolved in the CaCl₂ solution, and then the Na₂CO₃ was added to the solution to induce the simultaneous co-precipitation of the IONCs and the CaCO₃ cores formed by the CaCl₂ and Na₂CO₃ salts (Figure 1).

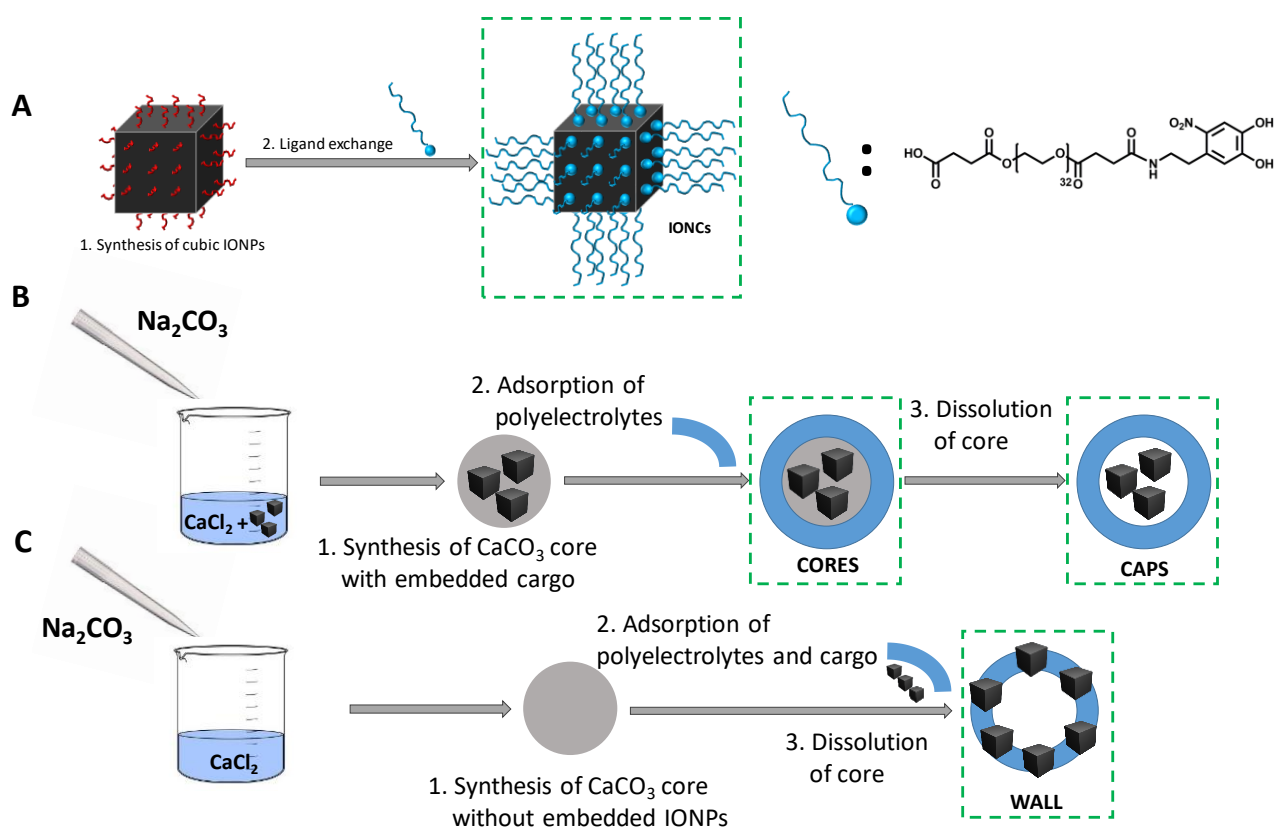


Figure 1: Sketch of the ligand exchange on the IONCs (A); The synthesis of calcium carbonate cores coated with polyelectrolytes with encapsulated IONCs, and polyelectrolyte capsules with IONCs in the cavity (B); The synthesis of polyelectrolyte capsules with embedded IONCs in the capsules' walls (C).

For the first submicrometric capsule arrangement, the magnetic CaCO_3 core (Figure 2B, F, J, S13) acted as a template for the subsequent decoration with polyelectrolyte shells using the Layer-by-Layer (LbL) procedure (Figure 2 B, F, J). The electrostatic attraction between the polyanionic and polycationic polymers allowed for the formation of polyelectrolyte multilayer assemblies, which could be followed by the inversion of the charge after addition of each subsequent layer (Figure S16). Since magnetic losses of IONCs are affected by a large number of parameters, one of which is the freedom to move under alternating magnetic fields H_{AC} in a colloidal dispersion, this first type of capsules was selected to spatially immobilize the IONCs in the CaCO_3 cores (CORE sample). A second type of capsule arrangement was made by selectively removing the CaCO_3 matrix, leaving the IONCs inside the hollow cavity, after having performed the LbL deposition (CAPS sample). In this case, given the removal of the CaCO_3 template, the IONCs can presumably physically move in the submicrocavity confinement.

Here, it is important to note that the IONCs were still protected within the shell of the capsules (Figure 2 C, G, K, Figure 3A, C, E, Fig. S11A). As a third type of capsule, IONCs were incorporated into the capsules' walls during the LbL assembly (WALL sample). In this instance, CaCO_3 cores were synthesized and the negatively

charged IONCs were placed in-between two consecutively positively charged polyelectrolyte layers during the LbL formation. At the end of the process, the CaCO_3 cores were dissolved. Also in this case, the IONCs were immobilized and protected from the external environment in-between the polymer layers (Figure 2 D, H, L, Figure 3B, C, E, Figure S11A). Indeed, the CaCO_3 is dissolved *via* calcium chelation with EDTA, forming an EDTA-Ca complex. Such a dissolution was confirmed and monitored by conducting an elemental analysis of calcium and iron before and after the addition of EDTA. The analysis shows that the Ca content of the CAPS sample decreased substantially up to 87 % with respect to the initial calcium amount that was found on the CORE sample. The Fe content was the same for the CORES and CAPS before and after the addition of EDTA, suggesting that no loss of capsule sample occurred during the EDTA reaction (Figure S17).

Using the above described approaches, eighteen magnetic nanostructures were prepared: five IONCs of different sizes (8 nm, 14 nm, 16 nm, 18 nm, 21 nm IONCs); three CORE capsules made of calcium carbonate cores with embedded IONCs of 14 nm, 16 nm, and 18 nm sizes, coated with four bilayers of polyelectrolytes; five CAPS capsules consisting of polyelectrolyte capsules with IONCs of different sizes (8 nm, 14 nm, 16 nm, 18 nm, and 21 nm) loaded in the inner cavity of the capsule; and five WALL polyelectrolyte capsules in which the IONCs of different sizes (8 nm, 14 nm, 16 nm, 18 nm, and 21 nm) were embedded into the capsule's layers (Figure 1). All capsules had a similar (dry) diameter of about 700 nm, as was determined by TEM measurements (Figure 2, S11A). In the case of CORES and CAPS, a monodisperse distribution of the IONCs within the capsules cavity was observed, indicating that the synthesis of the cores/capsules did not affect their stability as determined by TEM (Figure 2 inserts, S11A) and SEM analysis (Figure 3). It is also evident that the IONCs were successfully incorporated into the capsules' wall, since cubic structures can be seen along the whole shells of the capsules in Figure 2D, H, L, S11A. Size monodispersity was confirmed for all the magnetic nanostructures by optical bright field microscopy (Figure S12).

The capsules in aqueous solution have micrometer sized hydrodynamic diameters (see typical DLS spectra in Figure S14). Moreover, since the outer polyelectrolyte layer of the capsules is made of positive PAH polyelectrolyte, they have a positive ζ -potential, while the IONCs are negatively charged due to the carboxylic acid terminated PEG ligands (Figure S14). There are only slight variations in the hydrodynamic diameters of the CAPS and WALL loaded with IONCs (14 and 18 nm) (Table S1).

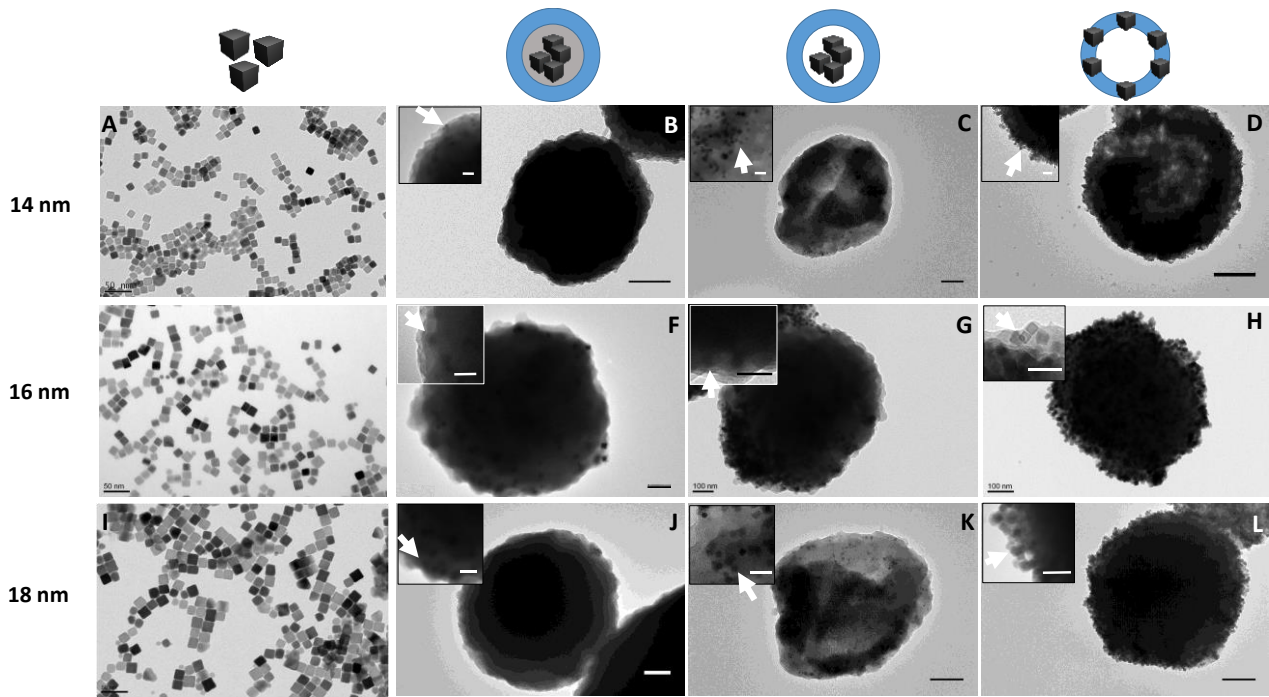


Figure 2: Representative TEM images of nitrodopamine-carboxy-PEGylated 14 nm IONCs (A); CORES with embedded 14 nm IONCs (B); CAPS capsules with embedded 14 nm IONCs (C); WALL capsules with embedded 14 nm IONCs (D); nitrodopamine-carboxy-PEGylated 16 nm IONCs (E); Core capsules with embedded 16 nm IONCs(F); CAPS capsules with embedded 16 nm IONCs (G); WALL capsules with embedded 16 nm IONCs (H); nitrodopamine-carboxy-PEGylated 18 nm IONCs (I); CORES with embedded 18 nm IONCs (J); CAPS capsules with embedded 18 nm IONCs (K); WALL capsules with embedded 18 nm IONCs (L). The scale bar of B, C, D, F, G, H, J, K, and L corresponds to 200 nm, while the scale bar of A, E, and I corresponds to 50 nm. . Insets are higher magnification images taken at the edge of the capsules. Scale bars of the insets correspond to 50 nm for all panels.

To gain more topographical and morphological information, and to elucidate the differences of IONC spatial distribution in the CAPS and WALL capsules, we have conducted a SEM analysis. The closer proximity of the IONCs (16 ± 2 nm) to the surface in the WALL samples confers a peculiar surface roughness for WALL sample with respect to CAPS (Figure 3C,D). Moreover, the bright signal, which is due to the backscattered electron signal of the IONCs, confirms that the IONCs were homogeneously distributed throughout the whole capsule in the CAPS sample (Figure 3A,C,E), whereas the bright spots of the IONCs are irregularly distributed in the capsules walls in the case of WALL sample (Figure 3B,D,F).

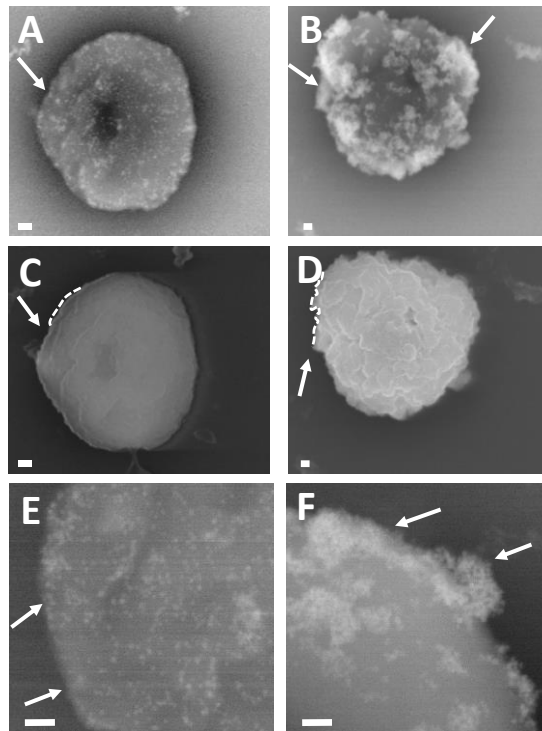


Figure 3: SEM images of the capsules prepared using a LbL procedure. A,B) Backscattered electron signal (BES) of the CAPS (left column) and the WALL (right column), showing the distribution of the IONCs (16 ± 2 nm) inside the capsules (COMPO mode). C,D) Secondary electron imaging (SEI) of the capsules, highlighting the different surface roughness of the CAPS and WALLS (middle row). E,F) Magnifications of the capsules' edges show an irregular surface roughness for WALL capsules (white arrows, F) in comparison to CAPS, where the bright spots of the IONCs are more distributed within the polymer (E). Scale bars correspond to 100 nm.

Hyperthermia measurements

The specific absorption rate (SAR) values of the IONCs and of all the synthesized capsules were measured by calorimetry at different frequencies (185 kHz and 302 kHz) and field intensities (28 and 24 kA/m), corresponding to field conditions close to and far from the biological limit ($H \cdot f = 5 \times 10^9 \text{ Am}^{-1}\text{s}^{-1}$, in which H is the amplitude of the magnetic field and f is the field frequency⁵¹). Figure 3 shows the SAR values that were obtained at 302 kHz and 24 kA/m for the free IONCs of different sizes (from 14 to 18nm) and the related capsules dispersed in water.

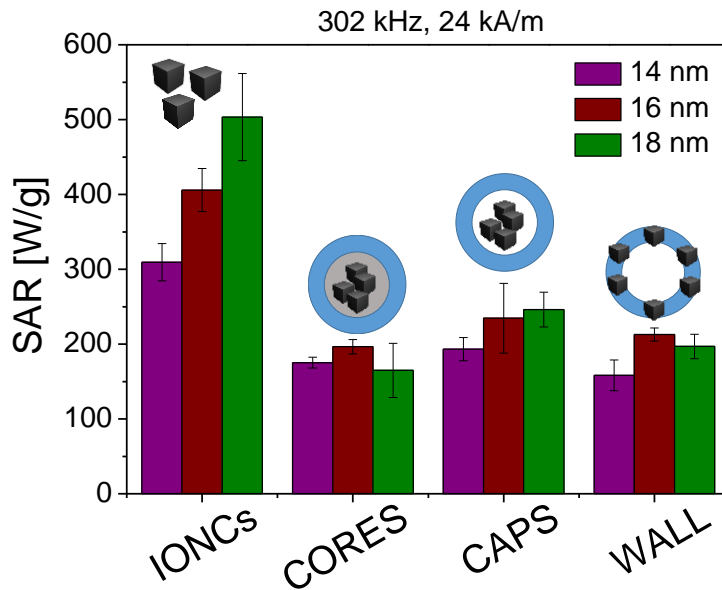


Figure 4: SAR values measured with the calorimetric method as obtained from free and encapsulated IONCs (CORES CAPS and WALL) dispersed in water for different IONC sizes.

As is shown in Figure 4, the highest SAR values in aqueous media were obtained for free IONCs, increasing with size. The related SAR values are comparable to those reported.^{9,15} However, SAR values obtained in the capsules (i.e., CORES, CAPS and WALL) resulted non-significant differences (given the large error bars of the calorimetric measurements). Thus, SAR values were reduced between 30% and 70%, inside capsules and depending on IONC size and encapsulation procedure albeit a little bit less for the CAPS. The reduction in magnetic losses for IONCs of different sizes in the different capsulation modalities showed similar SAR behavior, which became more pronounced when the IONC size is increased^{7,52} (Figure 4, S11, S18-S20). However, immobilization was not the only effect reducing the heating mechanism for the 14 nm IONCs, which were spatially confined into the CAPS, as also this sample showed a reduction in the SAR value (30%) with respect to free IONCs. This reduction in the SAR value was lower than in the capsules with randomly distributed IONPs, in which a drop of 50% was observed,³² underlining the relevance of the spatial control of the IONCs in the employed encapsulation approach. This SAR reduction increased with an increase in the IONCs' size, probably due to the prevalence of the Brownian relaxation that is significantly evident in the case of the CORES and WALLS samples. It is well known that aggregation may also strongly shrink magnetic heat losses when IONCs are embedded into capsules.³² Indeed, the interparticle distance and random spatial distribution of IONCs in the distinct capsule arrangements (CORES, CAPS and WALL) cause different magnetic dipolar interactions, which, may result in a reduction or increase of magnetic heat losses.^{53,54} Moreover, such magnetic dipolar interactions increase when the IONC size is increased, which is in agreement with our previous observations.¹⁶

In order to enlarge the range of sizes of IONCs, we tested the formation of capsules (CAPS and WALL types) using also 8 ± 1 nm and 21 ± 2 nm IONCs (Figure S11). We observe the same trend in terms of structural properties, *i.e.* morphology and colloidal parameters. Regarding the heating efficiency, indeed the 8 nm IONC sample was too small to provide measurable SAR under the same measuring conditions used for the other IONC and capsules samples (300 kHz and 24 kA/m and 1 g(Fe)/L), nor any of the systems of CAPS and WALL made with IONCs of 8 nm. With regard to the systems containing 21 nm IONCs, SAR values of IONCs in water are excellent (810 ± 7 W/g) and higher than any other system of CAPS or WALL samples presented in this work. Even after the encapsulation, associated to a certain decrease in SAR again probably due to the prevalence of the Brownian relaxation, the samples preserve high SAR values (CAPS: 380 ± 25 W/g, WALL: 490 ± 14 W/g). However, it is also worth to mention that for 21 nm IONCs, the yield of capsules is lower than that for the other capsule preparation (usually the yield is up to 30 % less than for the capsules samples made of IONCs with $D < 21$ nm). This may be due to magnetic interaction during the preparations that promotes fast precipitations of nanoparticles and less control on the protocol.

The common trend for encapsulated 14, 16 and 18 nm IONCs is clearly reflected in the dynamical hysteresis loops that were obtained under similar H_{AC} conditions (Figure 5, S25-S27).

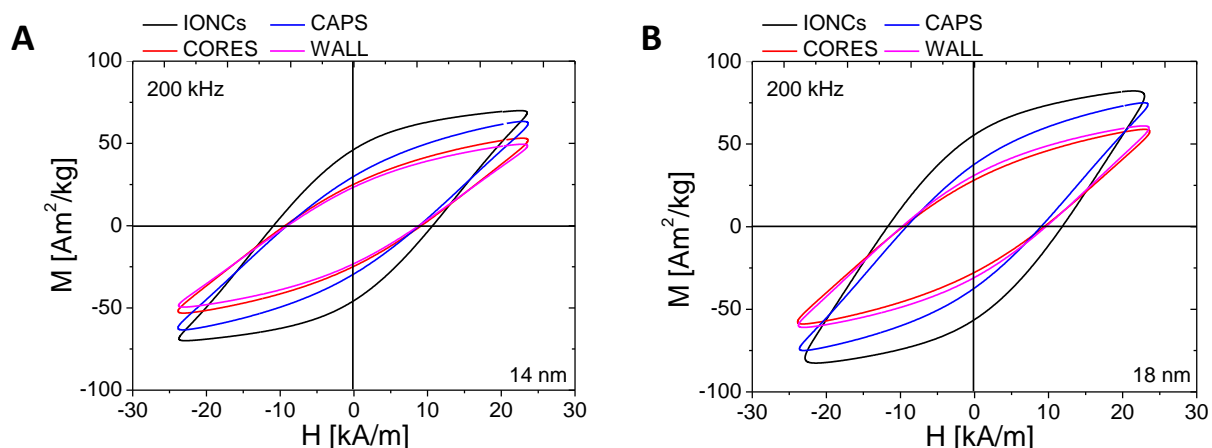


Figure 5: AC hysteresis loops of the different capsules and free IONCs dispersed in water at given iron content (1.5 g(Fe)/L), and field conditions (200 kHz and 24 kA/m) : (A) $d(\text{IONCs}) = 14$ nm; (B) $d(\text{IONCs}) = 18$ nm .

AC hysteresis loops are a direct and accurate method to probe and quantify the parameters that influence the magnetic losses.^{26,30,55} In agreement with calorimetry results, free 18 nm IONCs have the largest AC hysteresis loop opening, followed by CAPS (blue curve), CORES (red curve), and WALL (pink curve) samples, respectively. Confining the IONC within the capsules causes always a reduction on the related AC hysteresis loop opening. This confirms the same behavior as the SAR calorimetric values, independent of the IONC size (see, for instance, Figure 5A for 14 nm nanocubes). Moreover, as is indicated in Table S7, the area under the hysteresis loops always increased when the edge length (14, 16, 18 nm) of the IONCs was increased.

It is also worth to mention that hysteresis Area and SAR values measured at clinical conditions used for the treatment of glioblastoma multiforme (100 kHz and 24kA/m), are significant not only for the free nanocubes but also for all the capsule's samples (Table 1, in this latter cases the values are certainly reduced).

| | A(mJ/kg)/SAR(W/g) at 100 kHz and 24 kA/m |
|--------------|---|
| IONCs, 14 nm | 2329/233 |
| CORES, 14 nm | 1183/118 |
| CAPS, 14 nm | 1637/164 |
| WALL, 14 nm | 975/93 |
| IONCs, 18 nm | 3018/302 |
| CORES, 18 nm | 1249/125 |
| CAPS, 18 nm | 2004/200 |
| WALL, 18 nm | 1842/184 |

Table 1: Areas and SAR values obtained by AC magnetometry⁵⁶ from the distinct magnetic nanomaterials at clinical conditions (100 kHz and 24 kA/m).

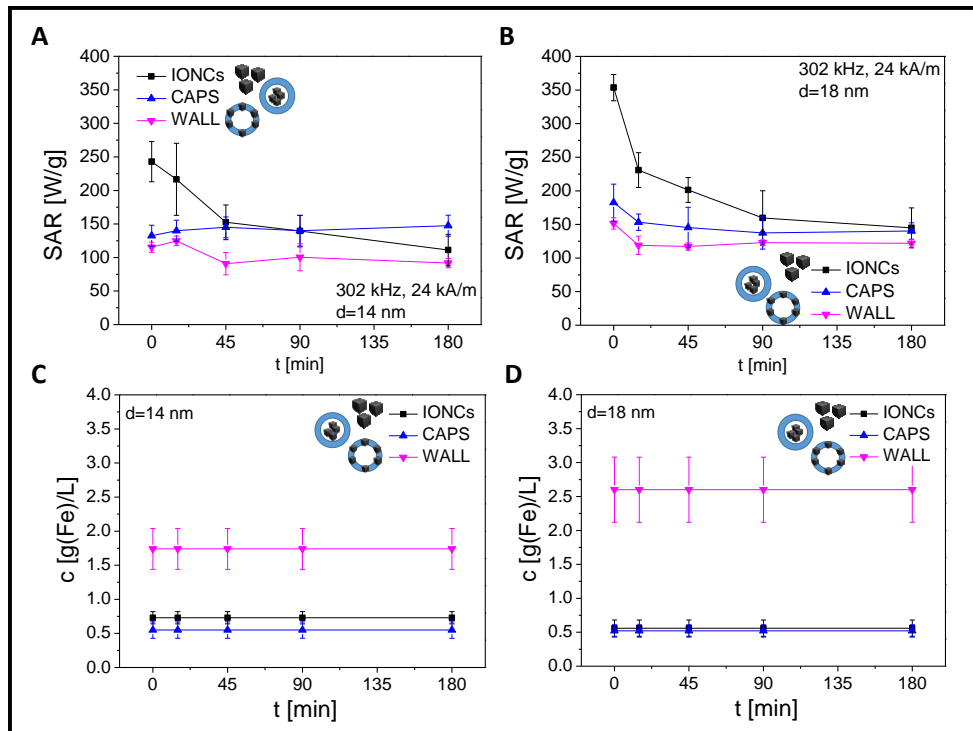
Probing the magnetic heating efficiency of magnetic materials inside cells

As previously mentioned, nanoparticle aggregation,^{30,57} immobilization³⁰ and degradation²⁸ occur when magnetic nanostructures interact with cells, resulting in significant variations in the heating efficiency with respect to the values that are obtained in colloidal dispersions. Their effects on the dynamical magnetic response should be avoided in order to control the physicochemical properties of the synthesized nanoparticles so that the heat dose supplied by the IONCs inside the cells or tissues can be preserved. To investigate how the encapsulation of IONCs in polymeric capsules may preserve the magnetic losses once associated to the cells, SAR values were measured during their interaction with the cells. For these experiments, we used both, CAPS capsules with IONCs inside the hollow cavity and WALL capsules in which the IONCs were randomly immobilized. In the latter case, since IONCs are immobilized at fixed at average interparticle distances inside the CORES capsules, no significant differences were expected in terms of heat efficacy. With regard to the capsules containing IONCs, we selected only the 14 and 18 nm IONCs. The SAR values were monitored after different incubation times (0, 15, 45, 90, 180 min). In the case of free IONCs (black curves), the SAR values drastically decreased to different extents depending on the nanoparticle size when the incubation time was increased (about 54% for 14 nm IONCs and 60% for 18 nm IONCs) (Figure 6A

and 6B). Only slight reductions in the SAR values (ca. 20 %) were observed for CAPS (blue curves) and WALL (pink curves) capsules, independent of the IONC size. Figure 6A and B show the variation in the SAR values for different magnetic nanostructures over time (< 3 h) .

Interestingly, after 180 min of incubation, the cells that have received IONCs were attracted to the magnet within 10 s, whereas pristine free IONCs (*i.e.* IONCs that were not incubated with cells) did not show any visible response to the magnetic field (Figure S28). This suggests that, after 3 h of incubation, the IONCs were associated with the tumour cells, which might be also promoted by electrostatic interactions and protein serum absorption on capsules and IONCs.^{58,59} A significant and progressive reduction of more than 50% was observed for free IONCs after just a few hours. During this period, the SAR values of capsules varied by less than 30%. It is important to highlight that no variations in the SAR values were obtained for CAPS and WALL capsules within the time frame of the study. However, for free IONCs, changes in the SAR were time dependent (see Table S8 for summary of SAR values from calorimetric measurements in cells). This is in agreement with the observations made by Di Corato et al.,⁹ who state that the SAR dynamics during the incubation of nanocubes and other types of iron oxide nanoparticles show a significant reduction in SAR values. Indeed, under this condition a fraction of the IONCs was associated with cell plasma membrane or internalized while a fraction of IONCs was still not yet internalized by the cells contributing more to the heating. The drop of SAR values over time is caused by the decrease of the fraction of free IONCs/capsules in the media and the increase of fraction of IONCs/capsules that were internalized/associated particles able to contribute to the heating efficiency.⁶⁰

in suspension



in adhesion

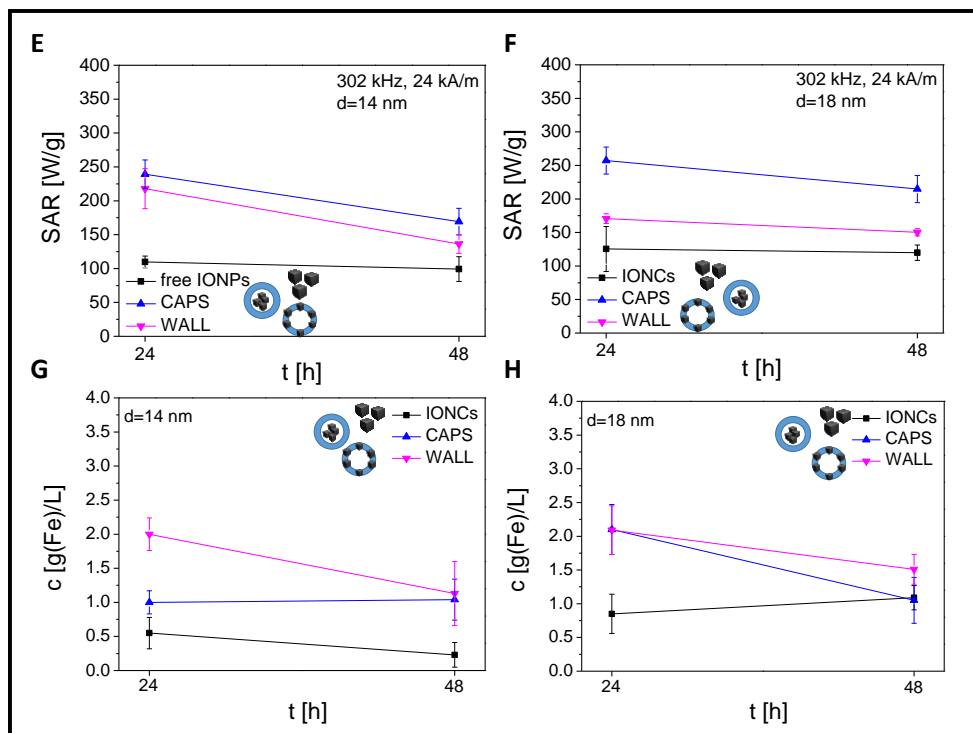


Figure 6: Time-dependent SAR values of free and encapsulated IONCs during incubation with cells at different time points at 302 kHz and 24 kA/m. A. $d(\text{IONCs}) = 14 \text{ nm}$, B. $d(\text{IONCs}) = 18 \text{ nm}$. Time-dependent iron concentration of IONCs associated with cells. C. $d(\text{IONCs}) = 14 \text{ nm}$, D. $d(\text{IONCs}) = 18 \text{ nm}$. Time-dependent SAR values of magnetic nanostructures during incubation with cells after 24 and 48 hours for E. $d(\text{IONCs}) = 14 \text{ nm}$ and F. $d(\text{IONCs}) = 18 \text{ nm}$. Time-dependent iron concentration of IONCs internalized by the cells G. $d(\text{IONCs}) = 14 \text{ nm}$, H. $d(\text{IONCs}) = 18 \text{ nm}$.

At longer incubation times, the magnetic heat losses of the different magnetic nanostructures studied here have similar trends: CAPS have higher SAR values, closely followed by WALL samples. For free 14 and 18 nm IONCs incubated for 24 or 48 hours, there was a strong decrease in the SAR values as compared to the SAR value of the capsule systems in water (about 68% for 14 nm IONCs and 76% for 18 nm IONCs). This effect was independent of the IONC size. For the CAPS and WALL capsules, the SAR values at 24 and 48 hours were similar and much larger than the free IONC values (Fig.6E and 6F). Nevertheless, a reduction in SAR values over time, ranging from 10% up to 30%, was observed depending on the IONC size. These data show that the magnetic losses of the CAPS and WALL capsules reduce more slowly inside cells and have higher values than free IONCs. The preservation of magnetic losses by the polyelectrolyte encapsulation fails with time. After 48 h, SAR values were lower than they were after 24 h, suggesting that an internalization of IONCs/capsules occurs, gradually causing sample aggregation. In the case of the capsules, which have a certain stiffness, their deformation with time after internalization likely favors an enhancement of intracellular IONC clustering, leading to a decrease in the SAR value.⁶¹

It is also worth noting that there is a difference in the SAR values for the free IONCs when the experiment was performed with the cells in suspension (short incubation time, Fig. 6A and 6B) and with adherent cells (long incubation, Figure 6E and 6F). Indeed, the SAR values for cells in suspensions were always higher than those for adherent cells. It could be that, at a short incubation time, a fraction of the IONCs were associated with cell plasma membrane while a large fraction of IONCs were still not yet internalized by the cells thus having the free IONCs contributing more to the heating. In the case of adherent cells, considering the longer incubation times, a larger fraction of IONCs is associated or internalized by the cells. This can explain why the SAR values that were measured for the free IONCs in suspension are higher than those for adherent cells.

However, SAR values obtained for CAPS and WALL capsules on adherent cells or on suspended cells are more directly comparable. A possible explanation is that the polymer layers of the capsules act as a sort of barrier to soften any changes in the environment, therefore the SAR is less dependent on the cellular association or internalization.

It is worth mentioning that IONCs and polyelectrolyte capsules were internalized by cells with a different rate. Given that the same amount of material was administered in terms of the amount of iron, it can be seen that, in terms of iron uptake, free IONCs were always taken up to a lesser extent than when they were packed in the capsules at 24 hours. This is reasonably due to the different charge of the free IONCs with respect to the CAPS and WALLS. Indeed, free IONCs are negatively charged while CAPS and WALL are positively charged (Figure S16). Previous works report that the positively charged nanoparticles are internalized by the cells at higher extent compared to the negatively charged ones,⁶²⁻⁶⁴ due to the higher interactions with the negatively charged cell membrane. Moreover, the PEG coating of IONCs may seriously decrease protein corona

formation and, thus, the reduce the interaction with cell plasma membrane.^{65,66} However, the amount of iron in the cells reaches the same amount for the 18 nm samples at 48 hours, while the amount of iron tends to decrease progressively with time for the free 14 nm nanocubes. Indeed, the amount of iron was significantly lower at 48 hours than that found in the same IONCs once they were incorporated into the cells (Figure 6C, 6D, 6G and 6H).

The intracellular localization of IONCs and capsules was studied using TEM images of the cells that had been exposed to the magnetic materials for 24 h of incubation at 37°C.⁵⁹ Figure 6 shows that the free IONCs accumulated inside the intracellular vesicles following a typical endocytic pathway.⁶⁷⁻⁶⁹ Very closed packed IONCs within the vesicles can be clearly seen, and these could be responsible for the observed decrease in the SAR of free cubic IONCs. Instead, CAPS capsules show a broader spatial distribution of IONCs with higher distances between them. In the case of WALL capsules, the darker elongated structures (black arrows) can be attributed to the walls of the polyelectrolyte capsules, which are decorated with IONCs in a darker color. With respect to the cells treated with the free IONCs, the lower density of the IONCs inside the hollow cavities or in the polymeric walls suggests that IONCs have a certain degree of freedom and that aggregation has been prevented to a certain extent.

All this evidence brings us to an important conclusion: the intracellular matrix does not alter the magnetic losses of IONCs when they are packed with the right configuration. This proves that a polyelectrolyte capsule shell can preserve IONCs from severe aggregation (*i.e.* the IONCs can still partly move, though there may be attractive van der Waals forces between them) and immobilization effects. Consequently, this can significantly alter the SAR values for free IONCs, as has often been reported in literature.⁹

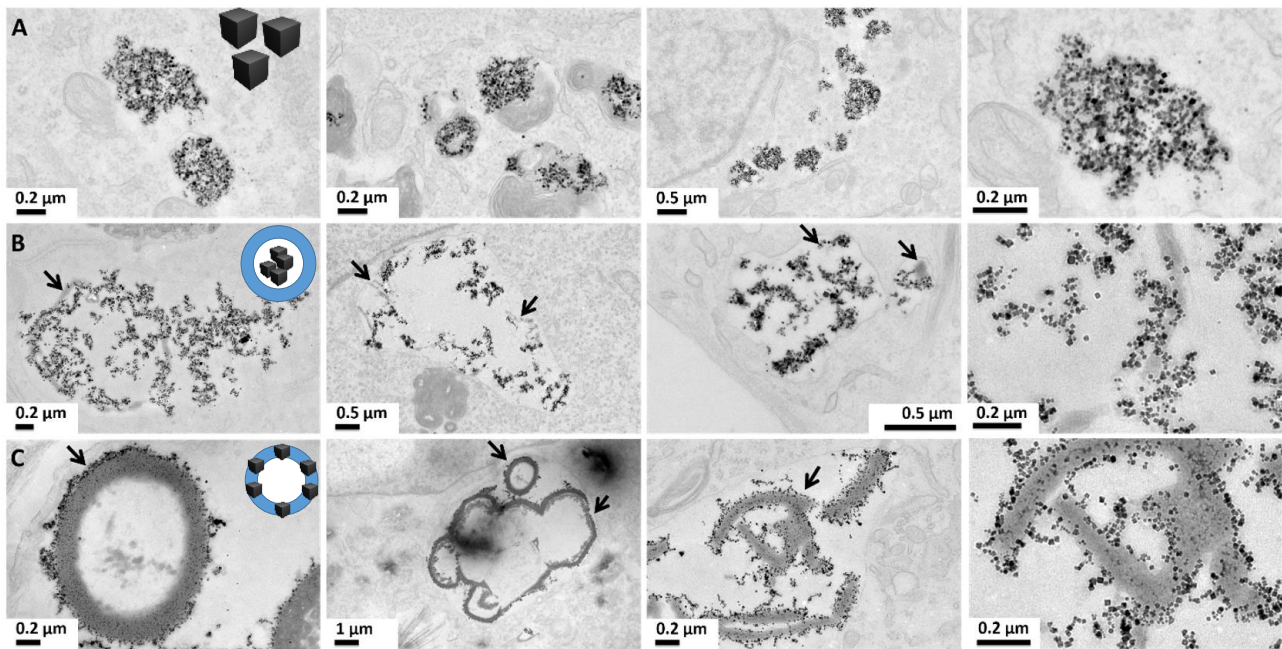


Figure 7: Representative TEM micrograph sections of SKOV-3 cells incubated for 24 h with: free 14 nm IONCs (Row A); CAPS (Row B); WALL (Row C.). The black arrows highlight the capsules' wall structures.

Influence of viscosity and aggregation on the magnetic response of free IONCs and capsules

To better understand the cell internalization effects on the magnetic heat losses of the different magnetic nanomaterials described above, we assessed the viscosity and aggregation effects on the SAR values of the different magnetic nanostructures studies dispersed in aqueous media.³⁰ The cellular association and further internalization of the IONCs/capsules further suppresses Brownian relaxation, since the IONCs/capsules cannot physically move. However, the aggregation of nanoparticles, which can take place on the cell plasma membrane or inside the endocytic vesicles, may also influence the Néel relaxation. To elucidate the effect of IONCs on membrane association, the first experiment that we set aimed to study the SAR behavior of the capsules in viscous media, which suppresses Brownian rotation. The SAR values were measured in different water-glycerol (W:Gly) mixtures set to 64:36 v% and 19:81 v%, corresponding to a mean η of 3.8 and 97.3 mPa·s respectively. As is shown in Figure 8 and Figures S21-S24, S31A, for the 14 nm IONC sample, the SAR values for the IONCs in water or in a glycerol solution are similar, indicating that the IONCs have a viscous independent SAR behavior. We would expect that the SAR values for the capsule samples (CORES, CAPS and WALL samples) would be similar to the SAR values of the initial IONCs, if no other immobilization effects occurs. However, the SAR values of all the capsules prepared with 14 nm IONCs are always lower than the SAR values of the 14 nm IONCs. This difference might be due to an additional immobilization or aggregation effect, which could occur when the IONCs are associated/incorporated into the capsules. This SAR reduction was also recorded for the other IONCs (16, 18 and 21 nm), but the dependency of the SAR on the viscosity in

these cases makes it more difficult to distinguish the effect due to the viscosity and the immobilization/aggregation effects in the capsules.

Moreover, the SAR value of free 18 nm IONCs decreased when there was an increase in the viscosity of the medium, whereas the SAR value remained constant at different viscosities for 14 nm IONCs. These results are in agreement with previous studies, which claim that the Brownian relaxation magnetic mechanism starts to have a significant contribution when the size of the IONCs is increased.^{16,26} Interestingly, for capsules with IONCs in the cavity, the SAR remained constant in the different viscous media, while it dropped slightly for capsules/cores with immobilized nanocubes (WALL and CORES). This suggests that IONCs in the cavity of the capsule had a certain freedom to move, and they remained more isolated by the environment. We might speculate that glycerol cannot enter through the capsules walls leaving the capsules mainly filled of water. Thus, the heat dissipation processes remained constant, and the heat efficiency of the capsules depended less on the viscous environment in which they were dispersed.

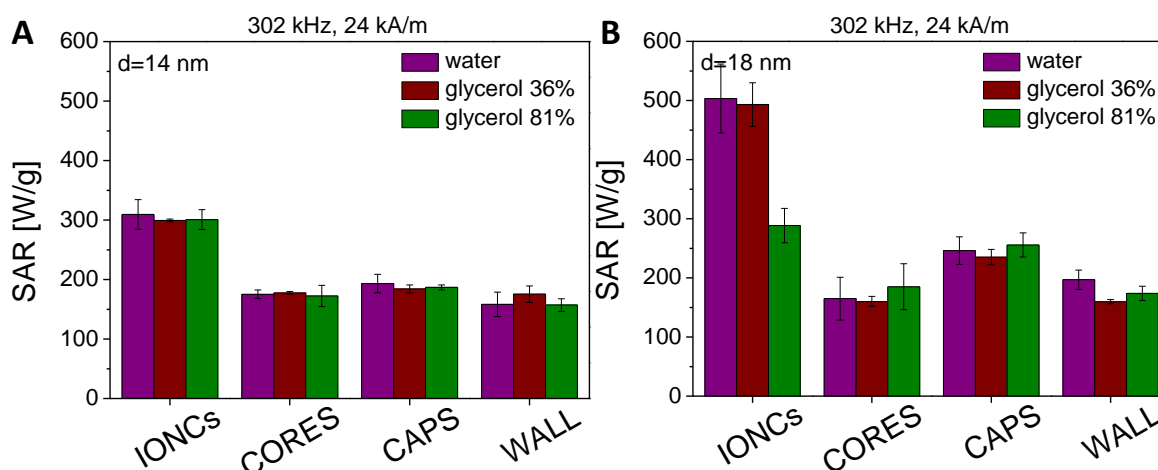


Figure 8: SAR values of different magnetic nanostructures dispersed in different viscous media at 320 kHz and 24 kA/m for (A) 14 nm IONCs and (B) 18 nm IONCs.

On the other hand, aggregation of the magnetic materials can occur during cell uptake, resulting in a reduction in SAR values. In order to study the aggregation effect, we intentionally induced nanoparticle/capsule aggregation by dispersing the samples in a concentrated phosphate buffer solution (PBS 5×, 0.05 M). The ions in the PBS solution contribute to screening the surface charge of colloids, so that van der Waals forces start to dominate and IONCs or capsules lose their colloidal stability and tend to aggregate.⁷⁰ The effect of the aggregation of the IONCs/capsules was determined from the SAR values that were obtained from the AC hysteresis loops (Figure S29, 30, 31B). As expected, a significant decrease in the SAR value of free IONCs was observed, with the aggregation in PBS (Figure 9) being more pronounced for 14 nm than for 18 nm IONCs. In contrast, the SAR values of capsules showed just slight variations when they were dispersed in PBS rather than in water (Figure 9). These findings strongly suggest that the capsule provide

a protective environment for the IONCs, preventing any increase in magnetic dipolar interactions *via* a reduction in the interparticle distances, therefore resulting in a reduction in magnetic losses.

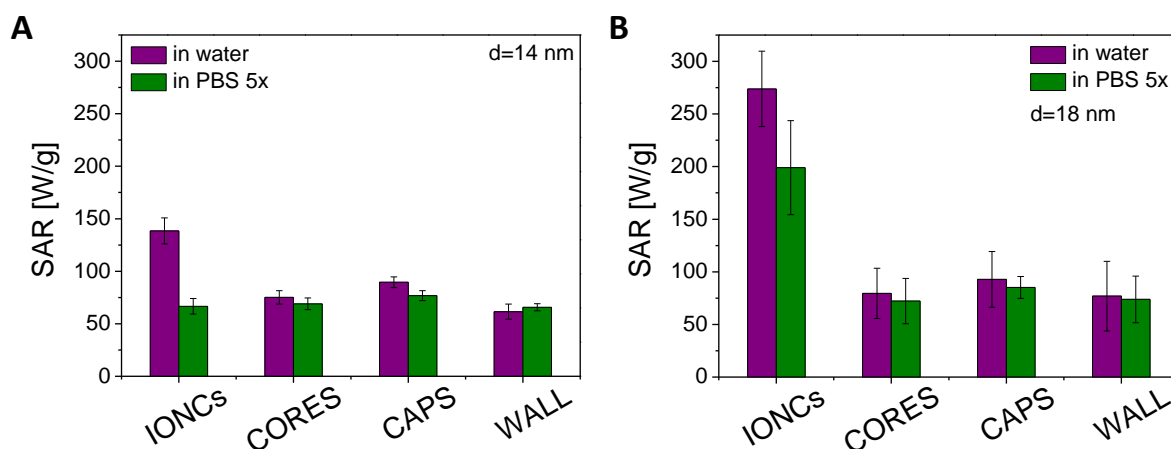


Figure 9: SAR values (areas under hysteresis loops \times frequency) of different magnetic materials dispersed in water and PBS 5x measured at 100 kHz, 24 kA/m (30 mT), 0.75 g(Fe)/L for (A) 14 nm IONCs and (B) 18 nm IONCs and their corresponding capsules.

Conclusions

Here, we report on an alternative procedure based on an encapsulation of IONCs in confined submicrocavities for preserving magnetic heat losses of IONCs inside cells. The comparison of SAR values between free IONCs and encapsulated IONCs in different spatial arrangements demonstrates that the magnetic losses of IONCs are maintained when the nanocubes are confined into the submicrocavities. This is the key results of this work and, indeed, as our study suggests, the confinement of nanocubes in submicrovolume protects the nanocubes from intra- and extracellular environment, which can negatively affect heating abilities of iron oxide nanocube, and, at the same time, prevents the nanocubes from endosomal aggregation.. Detailed studies show that, when the distinct capsules are exposed to H_{AC} after cell internalization, hollow capsules with IONCs in their cavity release higher amounts of magnetic heat than free IONCs and wall capsule configurations. The design of magnetic nanostructures whose dynamical magnetic response remains almost unaffected in a biological environment like the tumor cells is necessary for supplying a given intracellular heat dose. The employed encapsulation approach simplifies the methodology to determine the heat dose release from IONC into cells, since SAR values do not vary from colloid to intracellular environment. This study suggests that empty capsules loaded with magnetic nanoparticles into their cavities are the right nanoplatforms to preserve magnetic hyperthermia performance of outstanding nanocubes into any cellular matrix in a given time window (*i.e.* 24-48 hours).

Acknowledgements:

We thank Simone Nitti for nanocube preparation and Tiziano Catelani for TEM cellular sample preparation. M. V. Z was funded by the financial support of the EU- Initial Training Network Mag(net)icFun (PITN-GA-2012-290248). The part of this work related to the synthesis of submicrometric polymer capsules was founded with Russian Science Foundation, grant No. 19-75-00039 (M.V.Z.). This work was also partially funded by the AIRC project (Contract No. IG 20790), the European Research Council (starting grant ICARO, Contract No. 678109), the Deutsche Forschungsgemeinschaft (DFG grant PA 794/21-1), by the Spanish Ministry of Economy and Competitiveness (MAT2016-81955-REDT, SEV-2016-0686, MAT2017-85617-R) and Comunidad de Madrid (NANOFROTMAG-CM, S2013/MIT-2850). The European COST Action TD1402 (RADIOMAG), the President's Scholarship SP-1576.2018.4, and the Ramon y Cajal subprogram (RYC-2011-09617) are also acknowledged. Mr. Emilio J. Artés (Advanced Instrumentation Unit, iMdea Nanociencia) is acknowledged for his technical assistance. AE acknowledges Prof. Tobias Kraus and Prof. Eduard Artz (INM, Saarbrücken).

Literature

- (1) Hildebrandt, B.; Wust, P.; Ahlers, O.; Dieing, A.; Sreenivasa, G.; Kerner, T.; Felix, R.; Riess, H. The cellular and molecular basis of hyperthermia. *Crit. Rev. Oncol. Hematol.* **2002**, *43*, 33–56.
- (2) Wust, P.; Hildebrandt, B.; Sreenivasa, G.; Rau, B.; Gellermann, J.; Riess, H.; Felix, R.; Schlag, P. Hyperthermia in combined treatment of cancer. *Lancet Oncol.* **2002**, *3*, 487–497.
- (3) Jaque, D.; Martínez Maestro, L.; del Rosal, B.; Haro-Gonzalez, P.; Benayas, A.; Plaza, J. L.; Martín Rodríguez, E.; García Solé, J. Nanoparticles for photothermal therapies. *Nanoscale* **2014**, *6*, 9494–9530.
- (4) *Physics of Thermal Therapy: Fundamentals and Clinical Applications*; Moros, E., Ed.; Imaging in medical diagnosis and therapy; CRC/Taylor & Francis: Boca Raton, FL, 2013.
- (5) Périgo, E. A.; Hemery, G.; Sandre, O.; Ortega, D.; Garaio, E.; Plazaola, F.; Teran, F. J. Fundamentals and advances in magnetic hyperthermia. *Appl. Phys. Rev.* **2015**, *2*, 041302.
- (6) Ludwig, R.; Teran, F. J.; Teichgräber, U.; Hilger, I. Nanoparticle-based hyperthermia distinctly impacts production of ROS, expression of Ki-67, TOP2A, and TPX2, and induction of apoptosis in pancreatic cancer. *Int. J. Nanomedicine* **2017**, *12*, 1009–1018.
- (7) Deatsch, A. E.; Evans, B. A. Heating efficiency in magnetic nanoparticle hyperthermia. *J. Magn. Magn. Mater.* **2014**, *354*, 163–172.
- (8) Figuerola, A.; Di Corato, R.; Manna, L.; Pellegrino, T. From iron oxide nanoparticles towards advanced iron-based inorganic materials designed for biomedical applications. *Pharmacol. Res.* **2010**, *62*, 126–143.
- (9) Di Corato, R.; Espinosa, A.; Lartigue, L.; Tharaud, M.; Chat, S.; Pellegrino, T.; Ménager, C.; Gazeau, F.; Wilhelm, C. Magnetic hyperthermia efficiency in the cellular environment for different nanoparticle designs. *Biomaterials* **2014**, *35*, 6400–6411.
- (10) Guibert, C.; Dupuis, V.; Peyre, V.; Fresnais, J. Hyperthermia of magnetic nanoparticles: experimental study of the role of aggregation. *J. Phys. Chem. C* **2015**, *119*, 28148–28154.
- (11) Materia, M. E.; Guardia, P.; Sathya, A.; Pernia Leal, M.; Marotta, R.; Di Corato, R.; Pellegrino, T. Mesoscale assemblies of iron oxide nanocubes as heat mediators and image contrast agents. *Langmuir* **2015**, *31*, 808–816.
- (12) Lartigue, L.; Alloyeau, D.; Kolosnjaj-Tabi, J.; Javed, Y.; Guardia, P.; Riedinger, A.; Péchoux, C.; Pellegrino, T.; Wilhelm, C.; Gazeau, F. Biodegradation of iron oxide nanocubes: high-resolution *in situ* monitoring. *ACS Nano* **2013**, *7*, 3939–3952.

- (13) Kolosnjaj-Tabi, J.; Lartigue, L.; Javed, Y.; Luciani, N.; Pellegrino, T.; Wilhelm, C.; Alloyeau, D.; Gazeau, F. Biotransformations of magnetic nanoparticles in the body. *Nano Today***2016**, *11*, 280–284.
- (14) Espinosa, A.; Di Corato, R.; Kolosnjaj-Tabi, J.; Flaud, P.; Pellegrino, T.; Wilhelm, C. Duality of iron oxide nanoparticles in cancer therapy: amplification of heating efficiency by magnetic hyperthermia and photothermal bimodal treatment. *ACS Nano***2016**, *10*, 2436–2446.
- (15) Guardia, P.; Riedinger, A.; Nitti, S.; Pugliese, G.; Marras, S.; Genovese, A.; Materia, M. E.; Lefevre, C.; Manna, L.; Pellegrino, T. One pot synthesis of monodisperse water soluble iron oxide nanocrystals with high values of the specific absorption rate. *J. Mater. Chem. B***2014**, *2*, 4426.
- (16) Salas, G.; Camarero, J.; Cabrera, D.; Takacs, H.; Varela, M.; Ludwig, R.; Dähring, H.; Hilger, I.; Miranda, R.; Morales, M. del P.; et al. Modulation of magnetic heating via dipolar magnetic interactions in monodisperse and crystalline iron oxide nanoparticles. *J. Phys. Chem. C***2014**, *118*, 19985–19994.
- (17) Gleich, B.; Weizenecker, J. Tomographic imaging using the nonlinear response of magnetic particles. *Nature***2005**, *435*, 1214–1217.
- (18) Arami, H.; Khandhar, A. P.; Tomitaka, A.; Yu, E.; Goodwill, P. W.; Conolly, S. M.; Krishnan, K. M. In vivo multimodal magnetic particle imaging (MPI) with tailored magneto/optical contrast agents. *Biomaterials***2015**, *52*, 251–261.
- (19) Hensley, D.; Tay, Z. W.; Dhavalikar, R.; Zheng, B.; Goodwill, P.; Rinaldi, C.; Conolly, S. Combining magnetic particle imaging and magnetic fluid hyperthermia in a theranostic platform. *Phys. Med. Biol.***2017**, *62*, 3483–3500.
- (20) Gilchrist, R. K.; Medal, R.; Shorey, W. D.; Hanselman, R. C.; Parrott, J. C.; Taylor, C. B. Selective inductive heating of lymph nodes. *Ann. Surg.***1957**, *146*, 596–606.
- (21) Kossatz, S.; Grandke, J.; Couleaud, P.; Latorre, A.; Aires, A.; Crosbie-Staunton, K.; Ludwig, R.; Dähring, H.; Ettelt, V.; Lazaro-Carrillo, A.; et al. Efficient treatment of breast cancer xenografts with multifunctionalized iron oxide nanoparticles combining magnetic hyperthermia and anti-cancer drug delivery. *Breast Cancer Res.***2015**, *17*.
- (22) Moros, M.; Ambrosone, A.; Stepien, G.; Fabozzi, F.; Marchesano, V.; Castaldi, A.; Tino, A.; de la Fuente, J. M.; Tortiglione, C. Deciphering intracellular events triggered by mild magnetic hyperthermia *in vitro* and *in vivo*. *Nanomed.***2015**, *10*, 2167–2183.
- (23) Blanco-Andujar, C.; Walter, A.; Cotin, G.; Bordeianu, C.; Mertz, D.; Felder-Flesch, D.; Begin-Colin, S. Design of iron oxide-based nanoparticles for MRI and magnetic hyperthermia. *Nanomed.***2016**, *11*, 1889–1910.
- (24) K Kolosnjaj-Tabi, J.; Di Corato, R.; Lartigue, L.; Marangon, I.; Guardia, P.; Silva, A. K. A.; Luciani, N.; Clément, O.; Flaud, P.; Singh, J. V.; et al. Heat-generating iron oxide nanocubes: subtle “destructorators” of the tumoral microenvironment. *ACS Nano***2014**, *8*, 4268–4283.
- (25) Johannsen, M.; Gneveckow, U.; Eckelt, L.; Feussner, A.; Waldöfner, N.; Scholz, R.; Deger, S.; Wust, P.; Loening, S. A.; Jordan, A. Clinical hyperthermia of prostate cancer using magnetic nanoparticles: presentation of a new interstitial technique. *Int. J. Hyperth. Off. J. Eur. Soc. Hyperthermic Oncol. North Am. Hyperth. Group***2005**, *2*, 637–647.
- (26) Cabrera, D.; Lak, A.; Yoshida, T.; Materia, M. E.; Ortega, D.; Ludwig, F.; Guardia, P.; Sathya, A.; Pellegrino, T.; Teran, F. J. Unraveling viscosity effects on the hysteresis losses of magnetic nanocubes. *Nanoscale***2017**, *9*, 5094–5101.
- (27) Usov, N. A.; Liubimov, B. Y. Dynamics of Magnetic Nanoparticle in a viscous liquid: application to magnetic nanoparticle hyperthermia. *J. Appl. Phys.***2012**, *112*, 023901.
- (28) Mazuel, F.; Espinosa, A.; Luciani, N.; Reffay, M.; Le Borgne, R.; Motte, L.; Desboeufs, K.; Michel, A.; Pellegrino, T.; Lalatonne, Y.; et al. Massive intracellular biodegradation of iron oxide nanoparticles evidenced magnetically at single-endosome and tissue levels. *ACS Nano***2016**, *10*, 7627–7638.
- (29) Lévy, M.; Wilhelm, C.; Devaud, M.; Levitz, P.; Gazeau, F. How cellular processing of superparamagnetic nanoparticles affects their magnetic behavior and NMR relaxivity: Magnetic and NMR behaviors of cell-processed USPIO. *Contrast Media Mol. Imaging***2012**, *7*, 373–383.
- (30) Cabrera, D.; Coene, A.; Leliaert, J.; Artés-Ibáñez, E. J.; Dupré, L.; Telling, N. D.; Teran, F. J. Dynamical magnetic response of iron oxide nanoparticles inside live cells. *ACS Nano***2018**, *12*, 2741–2752.
- (31) Henriksen-Lacey, M.; Carregal-Romero, S.; Liz-Marzán, L. M. Current Challenges toward In vitro cellular validation of inorganic nanoparticles. *Bioconjug. Chem.***2017**, *28*, 212–221.

- (32) Ortgies, D. H.; Teran, F. J.; Rocha, U.; de la Cueva, L.; Salas, G.; Cabrera, D.; Vanetsev, A. S.; Rähn, M.; Sammelseg, V.; Orlovskii, Y. V.; et al. Optomagnetic nanoplatforms for In situ controlled hyperthermia. *Adv. Funct. Mater.* **2018**, *28*, 1704434.
- (33) Morales, M. P.; Bédard, M. F.; Roca, A. G.; Presa, P. de la; Hernando, A.; Zhang, F.; Zanella, M.; Zahoor, A. A.; Sukhorukov, G. B.; del Mercato, L. L.; et al. Relaxation times of colloidal iron platinum in polymer matrixes. *J. Mater. Chem.* **2009**, *19*, 6381.
- (34) Zyuzin, M. V.; Díez, P.; Goldsmith, M.; Carregal-Romero, S.; Teodosio, C.; Rejman, J.; Feliu, N.; Escudero, A.; Almendral, M. J.; Linne, U.; et al. Comprehensive and systematic analysis of the immunocompatibility of polyelectrolyte capsules. *Bioconjug. Chem.* **2017**, *28*, 556–564.
- (35) Hussain, S. Z.; Zyuzin, M. V.; Hussain, I.; Parak, W. J.; Carregal-Romero, S. Catalysis by multifunctional polyelectrolyte capsules. *RSC Adv.* **2016**, *6*, 81569–81577.
- (36) Timin, A. S.; Muslimov, A. R.; Zyuzin, M. V.; Peltek, O. O.; Karpov, T. E.; Sergeev, I. S.; Dotsenko, A. I.; Goncharenko, A. A.; Yolshin, N. D.; Sinelnik, A.; et al. Multifunctional scaffolds with improved antimicrobial properties and osteogenicity based on piezoelectric electrospun fibers decorated with bioactive composite microcapsules. *ACS Appl. Mater. Interfaces* **2018**, *10*, 34849–34868.
- (37) Zyuzin, M. V.; Timin, A. S.; Sukhorukov, G. Multilayer Capsules inside biological systems: state of the art and open challenges. *Langmuir* **2019**, *35*, 4747–4762.
- (38) Carregal-Romero, S.; Guardia, P.; Yu, X.; Hartmann, R.; Pellegrino, T.; Parak, W. J. Magnetically triggered release of molecular cargo from iron oxide nanoparticle loaded microcapsules. *Nanoscale* **2015**, *7*, 570–576.
- (39) Kantner, K.; Rejman, J.; Kraft, K. V. L.; Soliman, M. G.; Zyuzin, M. V.; Escudero, A.; del Pino, P.; Parak, W. J. Laterally and temporally controlled intracellular staining by light-triggered release of encapsulated fluorescent markers. *Chem. - Eur. J.* **2018**, *24* (9), 2098–2102.
- (40) Gomes, J.; Grunau, A.; Lawrence, A. K.; Eberl, L.; Gademann, K. Bioinspired, releasable quorum sensing modulators. *Chem Commun* **2013**, *49*, 155–157.
- (41) Gillich, T.; Acikgöz, C.; Isa, L.; Schlüter, A. D.; Spencer, N. D.; Textor, M. PEG-stabilized core–shell nanoparticles: impact of linear versus dendritic polymer shell architecture on colloidal properties and the reversibility of temperature-induced aggregation. *ACS Nano* **2013**, *7*, 316–329.
- (42) Riedinger, A.; Guardia, P.; Curcio, A.; Garcia, M. A.; Cingolani, R.; Manna, L.; Pellegrino, T. Subnanometer local temperature probing and remotely controlled drug release based on azo-functionalized iron oxide nanoparticles. *Nano Lett.* **2013**, *13*, 2399–2406.
- (43) Hühn, J.; Carrillo-Carrion, C.; Soliman, M. G.; Pfeiffer, C.; Valdeperez, D.; Masood, A.; Chakraborty, I.; Zhu, L.; Gallego, M.; Yue, Z.; et al. Selected standard protocols for the synthesis, phase transfer, and characterization of inorganic colloidal nanoparticles. *Chem. Mater.* **2017**, *29* (1), 399–461.
- (44) Parakhonskiy, B. V.; Foss, C.; Carletti, E.; Fedel, M.; Haase, A.; Motta, A.; Migliaresi, C.; Antolini, R. Tailored intracellular delivery via a crystal phase transition in 400 Nm vaterite particles. *Biomater. Sci.* **2013**, *1*, 1273.
- (45) Parakhonskiy, B. V.; Haase, A.; Antolini, R. Sub-micrometer vaterite containers: synthesis, substance loading, and release. *Angew. Chem. Int. Ed.* **2012**, *51*, 1195–1197.
- (46) Parakhonskiy, B.; Zyuzin, M. V.; Yashchenok, A.; Carregal-Romero, S.; Rejman, J.; Möhwald, H.; Parak, W. J.; Skirtach, A. G. The influence of the size and aspect ratio of anisotropic, porous CaCO₃ particles on their uptake by cells. *J. Nanobiotechnology* **2015**, *13*.
- (47) Connord, V.; Mehdaoui, B.; Tan, R.P.; Carrey, J.; Respaud, M. An air-cooled litz wire coil for measuring the high frequency hysteresis loops of magnetic samples—a useful setup for magnetic hyperthermia applications. *Rev Sci Instrum.* **2014**, *85*, 093904.
- (48) Wildeboer, R. R.; Southern, P.; Pankhurst, Q. A. On the reliable measurement of specific absorption rates and intrinsic loss parameters in magnetic hyperthermia materials. *J. Phys. Appl. Phys.* **2014**, *47*, 495003.
- (49) Wang, S.-Y.; Huang, S.; Borca-Tasciuc, D.-A. Potential sources of errors in measuring and evaluating the specific loss power of magnetic nanoparticles in an alternating magnetic field. *IEEE Trans. Magn.* **2013**, *49*, 255–262.

- (50) Mehdaoui, B.; Meffre, A.; Carrey, J.; Lachaize, S.; Lacroix, L.-M.; Gougeon, M.; Chaudret, B.; Respaud, M. Optimal size of nanoparticles for magnetic hyperthermia: a combined theoretical and experimental study. *Adv. Funct. Mater.* **2011**, *21*, 4573–4581.
- (51) Guardia, P.; Di Corato, R.; Lartigue, L.; Wilhelm, C.; Espinosa, A.; Garcia-Hernandez, M.; Gazeau, F.; Manna, L.; Pellegrino, T. Water-soluble iron oxide nanocubes with high values of specific absorption rate for cancer cell hyperthermia treatment. *ACS Nano* **2012**, *6*, 3080–3091.
- (52) Lévy, M.; Wilhelm, C.; Siaugue, J.-M.; Horner, O.; Bacri, J.-C.; Gazeau, F. Magnetically induced hyperthermia: size-dependent heating power of γ -Fe₂O₃ nanoparticles. *J. Phys. Condens. Matter* **2008**, *20*, 204133.
- (53) Niculăes, D.; Lak, A.; Anyfantis, G. C.; Marras, S.; Laslett, O.; Avugadda, S. K.; Cassani, M.; Serantes, D.; Hovorka, O.; Chantrell, R.; et al. Asymmetric assembling of iron oxide nanocubes for improving magnetic hyperthermia performance. *ACS Nano* **2017**, *11*, 12121–12133.
- (54) Branquinho, L. C.; Carrião, M. S.; Costa, A. S.; Zufelato, N.; Sousa, M. H.; Miotto, R.; Ivkov, R.; Bakuzis, A. F. Effect of Magnetic Dipolar Interactions on Nanoparticle Heating Efficiency: Implications for Cancer Hyperthermia. *Sci. Rep.* **2013**, *3*, 1-10.
- (55) Ovejero, J. G.; Cabrera, D.; Carrey, J.; Valdivielso, T.; Salas, G.; Teran, F. J. Effects of inter- and intra-aggregate magnetic dipolar interactions on the magnetic heating efficiency of iron oxide nanoparticles. *Phys. Chem. Chem. Phys.* **2016**, *18*, 10954–10963.
- (56) Mehdaoui, B.; Carrey, J.; Stadler, M.; Cornejo, A.; Nayral, C.; Delpech, F.; Chaudret, B.; Respaud, M. Influence of a transverse static magnetic field on the magnetic hyperthermia properties and high-frequency hysteresis loops of ferromagnetic FeCo nanoparticles. *Appl. Phys. Lett.* **2012**, *100*, 052403.
- (57) Levy, M.; Wilhelm, C.; Luciani, N.; Deveaux, V.; Gendron, F.; Luciani, A.; Devaud, M.; Gazeau, F. Nanomagnetism reveals the intracellular clustering of iron oxide nanoparticles in the organism. *Nanoscale* **2011**, *3*, 4402.
- (58) Zyuzin, M. V.; Yan, Y.; Hartmann, R.; Gause, K. T.; Nazarenius, M.; Cui, J.; Caruso, F.; Parak, W. J. Role of the protein corona derived from human plasma in cellular interactions between nanoporous human serum albumin particles and endothelial cells. *Bioconjug. Chem.* **2017**, *28*, 2062–2068.
- (59) Kastl, L.; Sasse, D.; Wulf, V.; Hartmann, R.; Mircheski, J.; Ranke, C.; Carregal-Romero, S.; Martínez-López, J. A.; Fernández-Chacón, R.; Parak, W. J.; et al. Multiple internalization pathways of polyelectrolyte multilayer capsules into mammalian cells. *ACS Nano* **2013**, *7*, 6605–6618.
- (60) Lak, A.; Cassani, M.; Mai, B. T.; Winckelmans, N.; Cabrera, D.; Sadrollahi, E.; Marras, S.; Remmer, H.; Fiorito, S.; Cremades-Jimeno, L.; et al. Fe²⁺ deficiencies, FeO subdomains, and structural defects favor magnetic hyperthermia performance of iron oxide nanocubes into intracellular environment. *Nano Lett.* **2018**, *18*, 6856–6866.
- (61) Bédard, M. F.; Munoz-Javier, A.; Mueller, R.; del Pino, P.; Fery, A.; Parak, W. J.; Skirtach, A. G.; Sukhorukov, G. B. On the Mechanical stability of polymeric microcontainers functionalized with nanoparticles. *Soft Matter* **2009**, *5*, 148–155.
- (62) Kim, B.; Han, G.; Toley, B. J.; Kim, C.; Rotello, V. M.; Forbes, N. S. Tuning payload delivery in tumour cylindroids using gold nanoparticles. *Nat. Nanotechnol.* **2010**, *5*, 465–472.
- (63) Bannunah, A. M.; Vllasaliu, D.; Lord, J.; Stolnik, S. Mechanisms of nanoparticle internalization and transport across an intestinal epithelial cell model: effect of size and surface charge. *Mol. Pharm.* **2014**, *11*, 4363–4373.
- (64) Oh, N.; Park, J.-H. Surface chemistry of gold nanoparticles mediates their exocytosis in macrophages. *ACS Nano* **2014**, *8*, 6232–6241.
- (65) Walkey, C. D.; Chan, W. C. W. Understanding and controlling the interaction of nanomaterials with proteins in a physiological environment. *Chem. Soc. Rev.* **2012**, *41*, 2780–2799.
- (66) Gref, R.; Lück, M.; Quellec, P.; Marchand, M.; Dellacherie, E.; Harnisch, S.; Blunk, T.; Müller, R. . ‘Stealth’ corona-core nanoparticles surface modified by polyethylene glycol (PEG): influences of the corona (PEG chain length and surface density) and of the core composition on phagocytic uptake and plasma protein adsorption. *Colloids Surf. B Biointerfaces* **2000**, *18*, 301–313.
- (67) Feliu, N.; Hühn, J.; Zyuzin, M. V.; Ashraf, S.; Valdeperez, D.; Masood, A.; Said, A. H.; Escudero, A.; Pelaz, B.; Gonzalez, E.; et al. Quantitative uptake of colloidal particles by cell cultures. *Sci. Total Environ.* **2016**, *568*, 819–828.

- (68) Rahmani, S.; Ashraf, S.; Hartmann, R.; Dishman, A. F.; Zyuzin, M. V.; Yu, C. K. J.; Parak, W. J.; Lahann, J. Engineering of nanoparticle size via electrohydrodynamic jetting. *Bioeng. Transl. Med.* **2016**, *1*, 82–93.
- (69) Iversen, T.-G.; Skotland, T.; Sandvig, K. Endocytosis and intracellular transport of nanoparticles: present knowledge and need for future studies. *Nano Today* **2011**, *6*, 176–185.
- (70) Zyuzin, M. V.; Honold, T.; Carregal-Romero, S.; Kantner, K.; Karg, M.; Parak, W. J. Influence of temperature on the colloidal stability of polymer-coated gold nanoparticles in cell culture media. *Small* **2016**, *12*, 1723–1731.